BROOKHAVEN NATIONAL LABORATORY

BNL-113364-2016
File # 94317

Differences in the Nature of Active Sites for Methane Dry Reforming and Methane Steam reforming over Nickel Aluminate Catalysts

Jessica L. Rogers, Michael C. Mangarella, Andrew D. D'Amico, James R. Gallagher, Michael R. Dutzer,

Eli Stavitski, Jeffrey T. Miller, Carsten Sievers

Submitted to ACS Catalysis

August 2016

Photon Sciences Department

Brookhaven National Laboratory

U.S. Department of Energy
USDOE Office of Science (SC),
Basic Energy Sciences (BES) (SC-22)

DISCLAIMER

Differences in the Nature of Active Sites for Methane Dry Reforming and Methane Steam Reforming over Nickel Aluminate Catalysts

Jessica L. Rogers[1,2,3], Michael C. Mangarella[1], Andrew D. D'Amico[4], James R. Gallagher[5], Michael R. Dutzer[1,2], Eli Stavitski[6], Jeffrey T. Miller[5,7], Carsten Sievers[1,2*]

[1] School of Chemical & Biomolecular Engineering, Georgia Institute of Technology, Atlanta, GA 30332, U.S.A.

[2] Renewable Bioproducts Institute, Georgia Institute of Technology, Atlanta, GA 30332, U.S.A.

[3]The Dow Chemical Company, Freeport, TX 77541, U.S.A.

[4] Micromeritics Instrument Corporation, Norcross, GA 30093, U.S.A.

[5] Argonne National Laboratory, Chemical Technology Division, Argonne, IL 60430, U.S.A.

[6] National Synchrotron Light Source II, Brookhaven National Laboratory, Upton, NY 11973, U.S.A.

[7]School of Chemical Engineering, Purdue University, W. Lafayette, IN 47907, U.S.A.

* Phone: +1-404-385-7685, Fax: +1-404-894-2866, Email: carsten.sievers@chbe.gatech.edu

Abstract

The Pechini synthesis was used to prepare nickel aluminate catalysts with the compositions $NiAl_4O_7$, $NiAl_2O_4$, and $Ni_2Al_2O_5$. The samples are characterized by N_2 physisorption, temperature programmed reduction (TPR), temperature programmed oxidation (TPO), X-ray diffraction (XRD), X-ray photoelectron spectroscopy (XPS), transmission electron microscopy (TEM), and X-ray absorption spectroscopy (XAS). Characterization results indicate unique structural properties and excellent regeneration potential of nickel aluminates. Prepared samples are tested when unreduced and reduced prior to reaction for methane dry reforming and methane steam reforming reactivity. $NiAl_2O_4$ in the reduced and unreduced state as well as $NiAl_4O_7$ in the reduced state are active and stable for methane dry reforming due to the presence of four-fold coordinated oxidized nickel. The limited amount of metallic nickel in these samples minimizes carbon deposition. On the other hand, the presence of metallic nickel is required for methane steam reforming. $Ni_2Al_2O_5$ in the reduced and unreduced state and $NiAl_2O_4$ in the reduced state are found to be active for methane steam reforming due to the presence of sufficiently small nickel nanoparticles that catalyze the reaction without accumulating carbonaceous deposits.

Keywords: Spinel, Synthesis gas, X-ray absorption spectroscopy, Coordination number, Regeneration

Introduction

Nickel catalysts supported on γ-Al_2O_3 have been extensively used for various high temperature applications, such as hydrogenation, hydrocarbon reforming, water gas shift

promotion, and ammonia decomposition.[1-5] One of the major challenges is the potential deactivation of these catalysts during high temperature reactions by sintering,[6,7] carbon deposition,[6-8] or loss of active sites due to formation of $NiAl_2O_4$.[9,10] The formation of supposedly inactive $NiAl_2O_4$ has been cited as a major mode of deactivation for supported Ni/Al_2O_3 catalysts.[9-11]

Recently, bulk materials of the formula AB_2O_4/ABO_3 have regained attention for reactions such as methane steam reforming,[12-14] partial oxidation of methane,[15-17] methane dry reforming,[7,16,18-21] oxidative coupling of methane,[22] automotive emissions control,[23,24] diesel steam reforming,[25,26] oxidative ethane dehydrogenation,[27] tetradecane reforming, [28] and tar reforming.[8] Spinels of the formula AB_2O_4 are widely accepted to have a structure similar to magnetoplumbites,[29-31] while materials of the formula ABO_3 are known as perovskites.[32] While it is generally proposed that nickel aluminates have an inverse spinel structure with nickel primarily occupying octahedral sites,[33-36] some studies have reported that nickel primarily occupies tetrahedral sites.[19,37] Further, it has been reported that at high temperatures the distribution of ions in the octahedral and tetrahedral sites can change,[19,35,38] indicating mobility of nickel within the host framework. These materials are of great interest for methane steam reforming and methane dry reforming reactions due to their resistance to sintering and the decreased formation of carbonaceous deposits.[16,28,30] The reactivity of AB_2O_4/ABO_3 materials has been ascribed to many mechanisms: ability of individual atoms within the bulk structure to move reversibly in and out lattice,[16,23] nanospinodal decomposition,[24,39] reactivity of oxygen contained within the material,[15,18,22,27,28,31,34] formation of metal nanoparticles within the bulk structure framework,[8,9,19,30,40,41] or formation of nickel oxide particles supported by the nickel aluminate structure.[20]

Several methods are commonly used to prepare mixed oxide catalysts: solid state reaction,[35] co-precipitation,[6,14,31,42,43] sol-gel method,[13,20,44] combustion synthesis,[19] alkoxide method,[17,18,24] and Pechini synthesis.[16,40,45] In the Pechini synthesis, metal precursors are incorporated into a polymeric resin, which is calcined in a subsequent step.[45] The method is very effective for providing uniform multicomponent oxides because the resin reduces differences in chemical reactivity of the different metal ions during the formation of the oxide. Therefore, the uniform composition is maintained when the resin gradually decomposes during calcination, and segregation of the mixed oxide is minimized.[46,47] Another advantage of the Pechini synthesis is a much lower calcination temperature is required for synthesis than that required for a solid state reaction to form the same multicomponent oxide.[36]

Numerous studies using nickel catalysts reported that the active species in reforming reactions are the reduced nickel metal particles.[8,9,19,21,41] Rivas et al. found that $LaNiO_3$ perovskites prepared by the Pechini synthesis exhibited the highest stability for methane steam reforming.[9] The stability was said to result from the formation of highly dispersed reduced nickel crystallites after reduction that remained in close contact with the La_2O_3 substrate. Enger et al. studied nickel aluminates prepared by wet impregnation for methane steam reforming.[41] They found that after reduction in hydrogen, nickel particles were formed and were able to activate methane at temperatures greater than 627 °C. Ribeiro et. al studied $NiAl_2O_4$ prepared by combustion synthesis for methane dry reforming.[19] They concluded that the reactivity of the nickel aluminate was due to the migration of nickel to the surface forming reduced nickel nanoparticles that co-existed with bulk $NiAl_2O_4$.

The present work investigates the activity and stability of well-defined nickel aluminates of three compositions prepared by Pechini synthesis. The materials are thoroughly characterized

using a suite of physicochemical techniques. The effect of the composition and structure of $NiAl_4O_7$, $NiAl_2O_4$, and $Ni_2Al_2O_5$ on the performance in methane steam reforming and methane dry reforming is examined. Most importantly, active sites for reforming reactions and the formation of carbonaceous deposits are identified.

Experimental

Materials

Chemicals used in the synthesis, $Ni(NO_3)_2 \cdot 6H_2O$ (99.999% trace metals basis), ethylene glycol (spectrophotometric grade, > 99 %), citric acid (ACS reagent, 99.5% purity), were used as received from Sigma-Aldrich. $Al(NO_3)_3 \cdot 9H_2O$ (ACS grade, 98+%) was used as received from Strem Chemicals. Nickel aluminates were benchmarked against a commercial 50 wt% Ni/α-Al_2O_3 (High Fuel^{TM}) catalyst purchased from Alfa Aesar. De-ionized water was used throughout this study. Methane (UHP), Nitrogen (UHP), and CO_2 (Research Grade) from Airgas were used during reactivity experiments without further purification. Argon (UHP), 10% H_2/Ar (UHP), Helium (UHP), and 10% O_2/He (UHP) from Airgas were used for the temperature-programmed reduction (TPR) and temperature-programmed oxidation (TPO) experiments.

Pechini Synthesis of Nickel Aluminate Catalysts

Nickel aluminates were synthesized using the Pechini synthesis.[46] The metal ions were chelated with citric acid and polyesterified with ethylene glycol forming a polymeric resin. The amount of nickel nitrate and aluminum nitrate used during synthesis was calculated based on the desired content of nickel and aluminum in the spinel structure. The metal nitrates to citric acid (citric acid: ($[Ni^{2+}] + [Al^{3+}]$)) ratio of 3:1 (molar basis) were added to 500 mL water and stirred until all components were visibly dissolved. The mixture was then heated to 70 °C and stirred for

an additional 30 minutes to ensure complete mixing and dissolution of the metal citrate complexes. Ethylene glycol was then added at 60 wt% relative to the amount of citric acid used, and the mixture was slowly heated to 120 °C. All of the water was allowed to evaporate until the polymeric resin was formed. The produced resin was aged for two days at room temperature prior to calcination to ensure homogeneity.

The resin was calcined using a gas hourly space velocity (GHSV) of 33 mL air $min^{-1}g_{resin}^{-1}$. The resin was first heated to 400 °C at a ramp rate of 5 °C/min and held at 400 °C for 1 hour until all ethylene glycol was removed. The mixed metal oxide was then further heated to 1000 °C at 5 °C/min and held for 1 h. The resulting mixed metal oxide was ground using a mortar and pestle and sieved to 75 – 90 μm for all subsequent experiments.

Methane Dry Reforming and Methane Steam Reforming Reactions

Reactivity tests were carried out under atmospheric pressure in a laboratory scale vertical plug flow reactor, which was operated isothermally (Lindberg Minimite furnace). Brooks mass flow controllers (model 4850) were used to supply gas feeds. Steam was generated in the setup using an ISCO syringe pump (model 500 D), which fed into a heated T-piece that utilized nitrogen as the sweep gas. Quartz beads were used in the T-piece to provide additional surface area to allow for complete volatilization of the water feed. To further ensure steady flow of steam, 4 feet of heated line were installed after the T-piece to provide additional residence time before the reactants entered the reactor. An online GC (Bruker 450 RGA) was used to analyze reactor effluents. The GC was equipped with a dual TCD and an FID. One TCD was used for quantification of hydrogen while the other quantified carbon monoxide, methane, carbon dioxide, and nitrogen. The FID was used to confirm methane quantification from the TCD.

Linear calibration curves were created for the FID and TCDs using various compositions (within the range of experimental concentrations) of CO_2, CH_4, H_2, and N_2, flowing through an empty reactor at standard reaction temperature and pressure. Reactor effluent samples were taken every 15 minutes. Thermal conversion was investigated by running reactions in an empty reactor tube and was found to be negligible in all experiments. Conversion levels obtained at different flow rates (at constant space time) and particle sizes showed no effect of these variables confirming mass transport effects were not present. A GHSV of 52,400 h^{-1} (CO_2/CH_4) was employed in methane dry reforming experiments and 65,500 h^{-1} (CO_2/CH_4/N_2) in methane steam reforming experiments (dry basis). When reduction was employed prior to reactivity tests, the samples were heated to 600 °C at 5 °C/min in 20 % H_2/ N_2 mixture and held for 2 hours before the temperature was increased to 700 °C. All reactivity tests were conducted at 700 °C for 12 h. In the case of methane dry reforming studies, the feed gas was stoichiometric carbon dioxide and methane. For methane steam reforming studies, the feed was 20% methane with balance nitrogen, and the steam-to-carbon ratio (S/C) was 2.4.

Physicochemical Characterization

Elemental Analysis

The metal content in each of the nickel aluminates were determined using inductively coupled plasma optical emission spectroscopy (ICP-OES). The ICP-OES measurements were carried out by Galbraith laboratories.

N_2 Physisorption

N_2 physisorption measurements were carried out using a Micromeritics ASAP 2020. Approximately 1.0 g of sample was used in each measurement. Samples were outgassed at 300

°C for 1 h prior to analysis. The surface area was calculated using the BET method and the pore size and volume using the BJH method applied to the desorption branch of the isotherm.[48]

TPR and TPO

TPR and TPO experiments were carried out on a Micromeritics AutoChem II 2920 equipped with a cold trap and a TCD detector. Approximately 0.15 g of sample was used in each set of experiments. Three sets of experiments were performed on each sample: TPR, TPR-TPO, and TPR- TPO-TPR2. During the TPR segment of each of the experiments, the sample was heated from 25 °C to 1000 °C (10 °C/min) and held at 1000 °C for 30 minutes in 10% H_2-Ar mixture (UHP), and hydrogen consumption was recorded. In experiments where TPO was performed after TPR, the sample was flushed under Ar (UHP) for 30 minutes at 900 °C and then cooled to 35 °C under argon flow. Subsequently, the carrier gas was changed to 10% O_2-He (UHP), and the sample temperature was ramped from 35 °C to 1000 °C (10 °C/min), and held for 30 minutes. In experiments where TPR2 was performed following TPO measurements, the sample was cooled in Ar from the final TPO temperature of 1000 °C to 50 °C and held for 30 minutes. The gas was then changed to 10% H_2-Ar, and the TPR measurement, as described before, was repeated. In the control experiment, TPR followed directly by TPO was performed as described above.

X-ray Diffraction (XRD)

Powder XRD patterns were measured on a Philips X'pert diffractometer equipped with an X'celerator module. Diffractograms were obtained with Cu Kα radiation from $2\theta = 10 - 90°$ with a step size of 0.0167°.

In-situ XRD

In-situ XRD reduction was performed at X18a beamline at the National Synchrotron Light Source in Brookhaven. XRD patterns were acquired with a Perkin-Elmer (PE) amorphous silicon area detector with 2048 × 2048 pixels and a 200 × 200 μm^2 pixel size. The X-ray photon energy was set to 20 keV. Before collecting the diffractograms, the detector was calibrated using a LaB_6 standard. For each spectrum, 10 exposures of 4 s duration were recorded for both the diffraction pattern and the dark current, and the dark current was subtracted. A Clausen cell,[49] which allows for the flow of hydrogen over the sample, was used for acquisition of XRD data. The sample powder was loosely packed into a 1.0 mm o.d./0.9 mm i.d. quartz capillary. The capillary was connected to 1/16 inch Swagelok style fittings with Vespel ferrules. An Omega thermocouple was inserted into the capillary and placed adjacent to and contacting the catalyst bed. Plots of the 2θ data were created from the recorded XRD patterns using the Datasqueeze software developed by Paul Heiney. Collected data was converted to Cu Kα energy.

Transmission Electron Microscopy (TEM)

TEM, high angle annular dark field (HAADF) scanning transmission electron microscopy (STEM) images, and energy dispersive x-ray (EDX) spectrometry were collected using an FEI Tecnai F30 super twin field emission gun TEM. The TEM was operated at 300 keV and was equipped with a single tilt tomography holder from Fischione Instrument.[50] The samples for TEM observations were prepared by creating a powder-ethanol mixture that was added drop wise to 200 mesh copper grids with carbon film TEM grids.

Carbon Content

Spent catalysts were analyzed for carbon content by Galbraith laboratories using GLI procedure ME-14.

X-ray Photoelectron Spectroscopy (XPS)

XPS measurements were performed on a Thermo K α XPS equipped with a monochromatic small-spot X-ray source using an aluminum anode Al Kα (hv = 1486.6 eV). A background pressure was 4.9×10^{-8} bar, and 4×10^{-7} bar argon was used during measurement to prevent sample charging. Binding energies were referenced to the sample stage, which contains built in calibration standards of copper, silver, and gold.

X-ray Absorption Spectroscopy (XAS)

EXAFS and XANES Ni K-edge spectra were collected at beamline 9-BM-C at the Advanced Photon Source at Argonne National Laboratories (Proposal GUP-38563). A Si(1 1 1) double monochromator was used to select the beam energy for all measurements. The beam size was 800 × 1000 μm. Samples were pressed into wafers 4 mm in diameter using a cylindrical wafer press that contains 6 slots that can accommodate samples. The beam was internally calibrated with a metallic Ni reference foil, and spectra were collected in transmission mode. A spectrum was first taken of each of the fresh samples. The samples were then reduced at 900 °C in 5% H_2/Ar for 2 h in an external furnace. The samples were then flushed with nitrogen, cooled to room temperature, and the Ni-K edge spectra were obtained without exposing the sample to air. Reduced samples were then re-oxidized at 900 °C for 2 h in external furnace, flushed with nitrogen, cooled to room temperature, and the Ni-K edge spectra were obtained without exposing the sample to air. Next, fresh samples were heated to 700 °C in inert gas. The samples were then exposed to a stoichiometric $CH_4 – CO_2$ mixture for 1 h. The samples were then flushed with nitrogen, cooled to room temperature, and the Ni-K edge spectra were obtained without exposing the sample to air.

Data was analyzed using WinXAS. Two polynomial fits were used for background correction. For the pre-edge region, a linear fit was used and for the post edge, a cubic spline. The edge energy, E_0, was identified from the inflection point in the edge, i.e., the first maximum in the first derivative of the XANES spectrum. EXAFS data was then converted to k space using mue-fit function with 6 spline nodes and k^2 weighting. The Fourier transform of the k^2 weighted EXAFS oscillation (Δ k = 2.7 – 10.9) converted the data from k-space to R-space to obtain a radial distribution function. The peak of interest was isolated using inverse Fourier transform. The data was curve fitted by standard methods using experimental phase shift and backscattering amplitudes derived from standard compounds of known structure, Ni foil (12 Ni–Ni at 2.49 Å) and NiO (6 Ni–O at 2.09 Å). Difference spectra were created by subtracting reaction spectra from the as-is spectra.

Results

Physiochemical Properties of Prepared Catalysts

The nickel and aluminum concentrations in the nickel aluminate samples were determined by ICP-OES (Table 1). Stoichiometric nickel aluminate ($NiAl_2O_4$) has 33.2 wt% Ni. To maintain charge neutrality, the sample with 20 wt % nickel was designated $NiAl_4O_7$, the sample with 34 wt% nickel as $NiAl_2O_4$, and the sample with 45 wt% nickel as $Ni_2Al_2O_5$.

Table 1 - Characterization of nickel aluminates by elemental analysis, ammonia TPD, N_2 physisorption, temperature-programmed reduction, and temperature-programmed oxidation.

Sample	**$NiAl_4O_7$**	**$NiAl_2O_4$**	**$Ni_2Al_2O_5$**
Ni content [a] (wt%)	20	34	45
Al content [a] (wt%)	36	31	20
Surface area [b] (m^2/g)	41	37	25
Pore volume [c] (cm^3/g)	0.08	0.06	0.05
Pore diameter [d] (nm)	5	7	6
TPR H_2 uptake [e] (mmol/g)	3.3	5.5	7.6
TPO O_2 uptake [f] (mmol/g)	1.4	2.1	3.1
TPR2 H_2 uptake [e] (mmol/g)	3.3	5.5	7.6

[a] Elemental analysis determined from ICP-OES at Galbraith laboratories
[b] Calculated from N_2 physisorption data using the BET equation
[c] Calculated from N_2 physisorption data using the BJH equation applied to the desorption branch of the adsorption isotherm
[d] Calculated from N_2 physisorption data using 4V/A from BJH
[e] Total H_2 consumption from TPR data
[f] Total O_2 consumption from TPO data from 35 °C to 1000 °C

Nitrogen Physisorption

The surface area, pore volume, and pore size of all catalysts was determined by N_2 physisorption (Figure S1, Table 1). From the IUPAC classification all isotherms are type IV indicating a mesoporous solid.[48] The isotherm of $NiAl_4O_7$ showed a H2 hysteresis indicating

complex pores with ill-defined shape and size. The isotherm for $NiAl_2O_4$ contained a H1 hysteresis, which is representative of a narrow distribution of uniform (cylindrical) pores.[48] The isotherm for $Ni_2Al_2O_5$ contained a H4 hysteresis, which is attributed to the presence of narrow slit like pores. The presence of less than stoichiometric amount of nickel ($NiAl_4O_7$) caused irregularities in the spinel structure. A stoichiometric amount of nickel ($NiAl_2O_4$) created an ordered, uniform spinel structure. When the nickel content was increased further ($Ni_2Al_2O_5$) the pores of the spinel structure became narrower. This might be caused by the accumulation of nickel or nickel oxide particles in void spaces of the slit-like pores. For all samples, the majority of the pore volume is distributed amongst pores between 4 nm - 30 nm. The total pore volume decreased with increasing nickel content (Figure S2).

Temperature Programmed Reduction (TPR) and Temperature Programmed Oxidation (TPO)

$NiAl_4O_7$, $NiAl_2O_4$, and $Ni_2Al_2O_5$ exhibited high temperature reduction peaks corresponding to reduction of nickel aluminate species at 870 °C, 780 °C, and 800 °C, respectively (Figure 1). $NiAl_2O_4$ had a small peak at 360 °C corresponding to nickel oxide that exists on the surface of the bulk structure. $Ni_2Al_2O_5$ exhibited a large bimodal peak centered at 480 °C corresponding to the reduction of two different types of NiO that existed on the surface of bulk aluminate.[51,52] The area of the low temperature peak was approximately half of the total hydrogen consumed, indicating a NiO: $NiAl_2O_4$ ratio of about 1. All samples also exhibited a small shoulder at 960 °C. The values of hydrogen consumption (Table 1) corresponded to almost complete reduction of all nickel present in the samples. The assignment of $NiAl_2O_4$ was further validated by the TPR, where the measured value of H_2 consumption was 5.5 mmol H_2/g and the theoretical value was 5.7 mmol H_2/g (Figure S3).

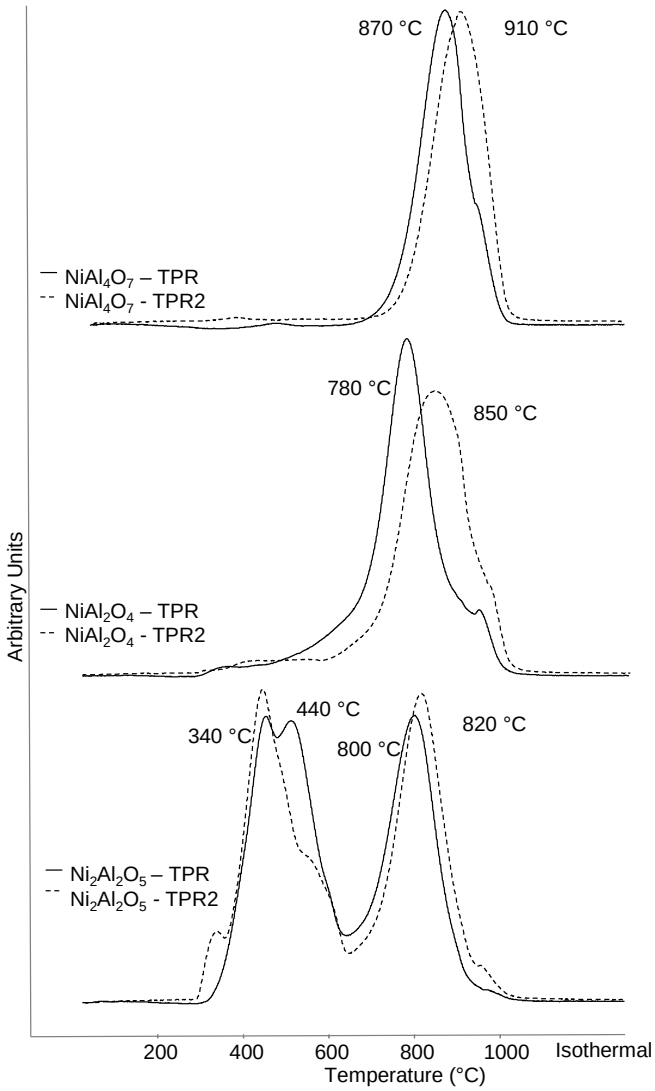

Figure 1 – Temperature programmed reduction of $NiAl_4O_7$, $NiAl_2O_4$, and $Ni_2Al_2O_5$. For fresh samples (solid lines) and after TPO (dashed lines).

Temperature programmed oxidation was performed on the samples after temperature programmed reduction (Figure 2). The total quantities of oxygen consumption (Table 1) indicated that $NiAl_4O_7$ was 84% re-oxidized, $NiAl_2O_4$ was 76% re-oxidized, and $Ni_2Al_2O_5$ 80% re-oxidized assuming an H_2/O_2 stoichiometry of 2/1. However, the calculated extent of re-oxidation is lower than the actual extent of reduction because oxygen uptake at room temperature

was excluded in the integration of the TPO profile as the starting temperature of the TPO was approximately 35 °C. The TPO profiles showed that oxidation occurred as soon as the temperature is increased, indicating that some oxidation has likely already taken place. For $NiAl_2O_4$, approximately 10% additional oxygen consumption was measured, in a separate isothermal chemisorption experiment, at 35°C. The presence of low and high temperature O_2 consumption peaks indicated that multiple types of nickel were present in the samples. $NiAl_4O_7$ showed a broad low-temperature oxidation peak at 440 °C and a small, high-temperature oxidation peak at 970 °C. $NiAl_2O_4$ had a primary oxidation peak at 320 °C and two smaller peaks at 900 °C and 1000 °C. $Ni_2Al_2O_5$ showed a low temperature peak at 380 °C and two higher temperature peaks at 850 °C and 1000 °C.

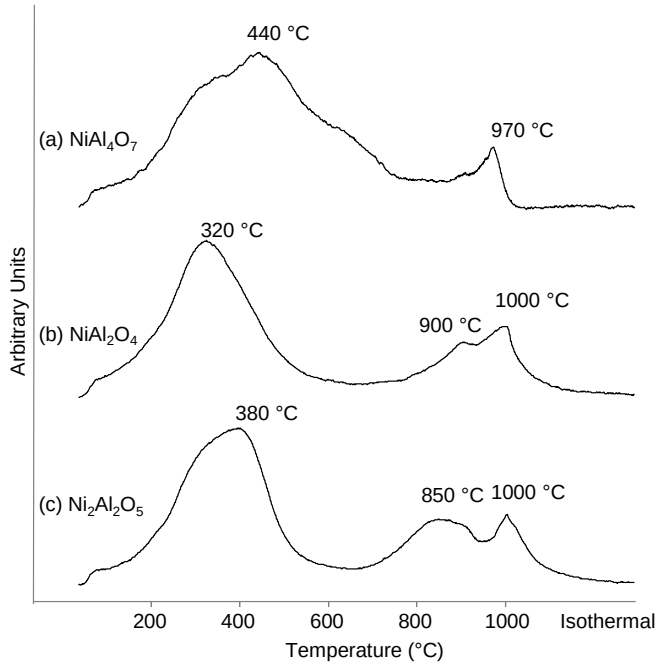

Figure 2 – Temperature programmed oxidation (TPO) of nickel aluminates.

Finally, the samples were exposed to a second TPR treatment (TPR2) after TPO (Figure 1 – dashed lines). The values of H_2 uptake (Table 1) were identical to the initial TPR indicating that the materials were oxidized to their original level of oxygen content. The reduction temperature for bulk aluminate species increased by 40 °C for $NiAl_4O_7$, 70 °C for $NiAl_2O_4$, and 20 °C for $Ni_2Al_2O_5$. For $Ni_2Al_2O_5$ the bimodal peak exhibited during TPR narrowed during TPR2 and is attributed to agglomeration of nickel species in this sample during the preceding treatment steps.

X-ray Diffraction (XRD)

XRD measurements were performed on fresh samples and after TPR, TPO, and TPR2 experiments. The dominating peaks in the diffractograms of fresh $NiAl_4O_7$, $NiAl_2O_4$, and $Ni_2Al_2O_5$ (Figure 3) were matched to a $NiAl_2O_4$ phase using HighScore Plus and the International Centre for Diffraction Data (ICDD) database. The diffractogram of $Ni_2Al_2O_5$ also exhibited additional peaks corresponding to NiO. After the TPR experiment, only metallic nickel was observed in the diffractograms. This phase may also be present, but undetectable, in fresh and oxidized samples due to the overlap of the XRD peaks of bulk $NiAl_2O_4$. XRD of samples after TPR, TPO, and TPR2 demonstrate the mobility of nickel in the nickel aluminate structure by the ability of the material to return to a state similar to the fresh sample after high temperature treatments.

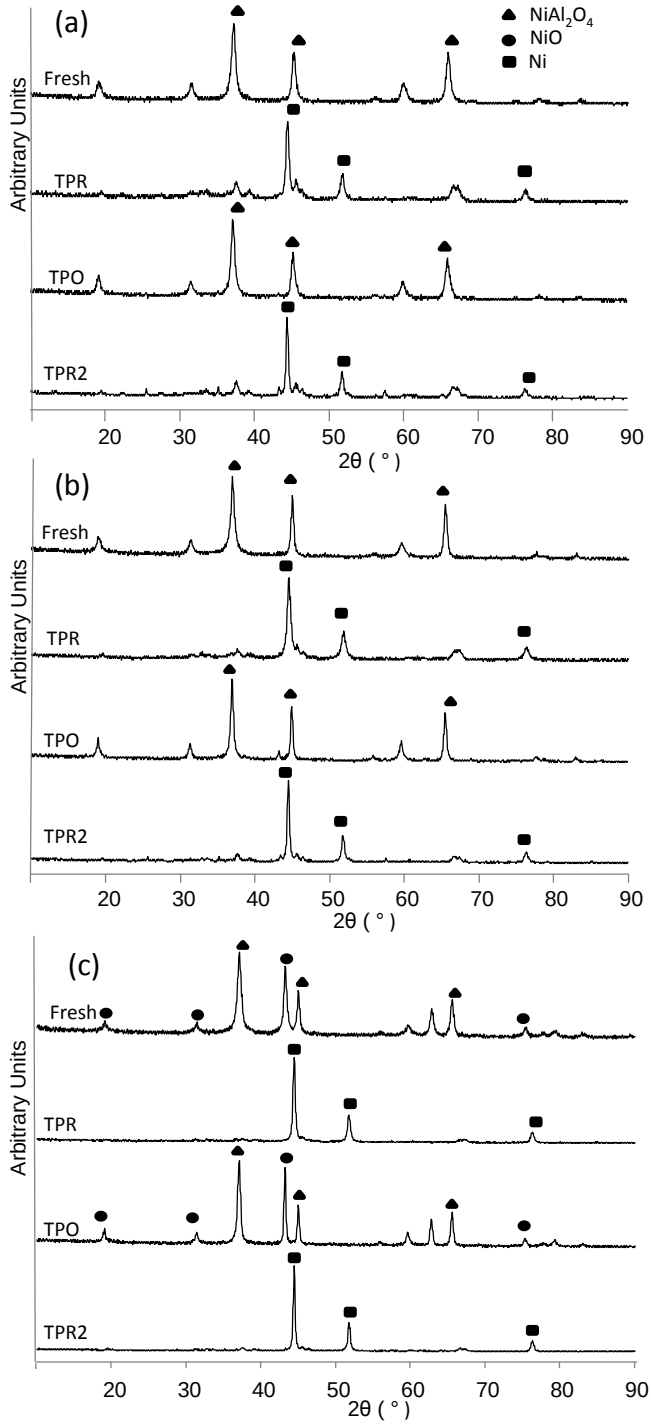

Figure 3 - XRD of (a) $NiAl_4O_7$ (b) NiA_2O_4 (c) $NiAl_2O_5$ after various treatments.

Samples were exposed to a hydrogen atmosphere, and the temperature of the XRD reactor was incrementally increased to the maximum temperature of the apparatus (T = 700 °C)

to collect in-situ XRD patterns. No change in crystallite structure was observed for $NiAl_4O_7$ or $NiAl_2O_4$ (Figures S2 and S3, respectively), as expected, based on high temperature reduction peaks indicated by TPR. For $Ni_2Al_2O_5$, formation of metallic nickel was observed in the presence of hydrogen as low as 650 °C (Figure 4).

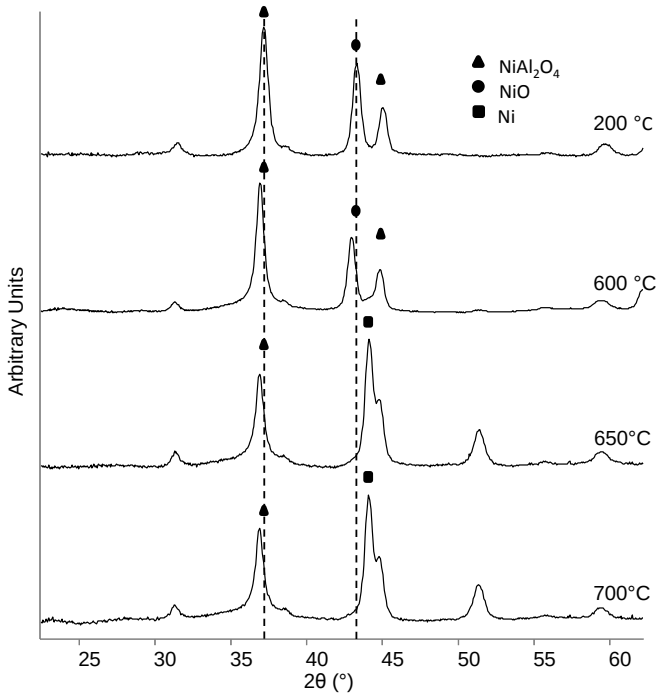

Figure 4 - $Ni_2Al_2O_5$ exposed to hydrogen as a function of increasing temperature.

Transmission Electron Microscopy

Bright field TEM images were collected for $Ni_2Al_2O_5$ (Figure 5a), $NiAl_4O_7$ (Figure 5b) and $NiAl_2O_4$ (Figure 5c,d). Pores and voids can be easily identified in the TEM images of $NiAl_2O_4$ and $NiAl_4O_7$. Note that the black spots result from strong diffraction of particles with a specific orientation to the electron beam.[53] They are not indicative of a specific composition of the particles. Grain sizes were calculated using dark field TEM images (Figure S6), which allowed ease of identification of individual grains due to the increased contrast. High angle annular dark field (HAADF) scanning transmission electron micrographs (STEM) were acquired, and energy dispersive X-ray spectrometry (EDX) was performed (Table 2, Figures S7-S9). The atomic composition was found to be similar to that obtained using ICP-OES (Table 1) with the differences in oxidation attributed to the sample size used during the STEM-EDX measurement.

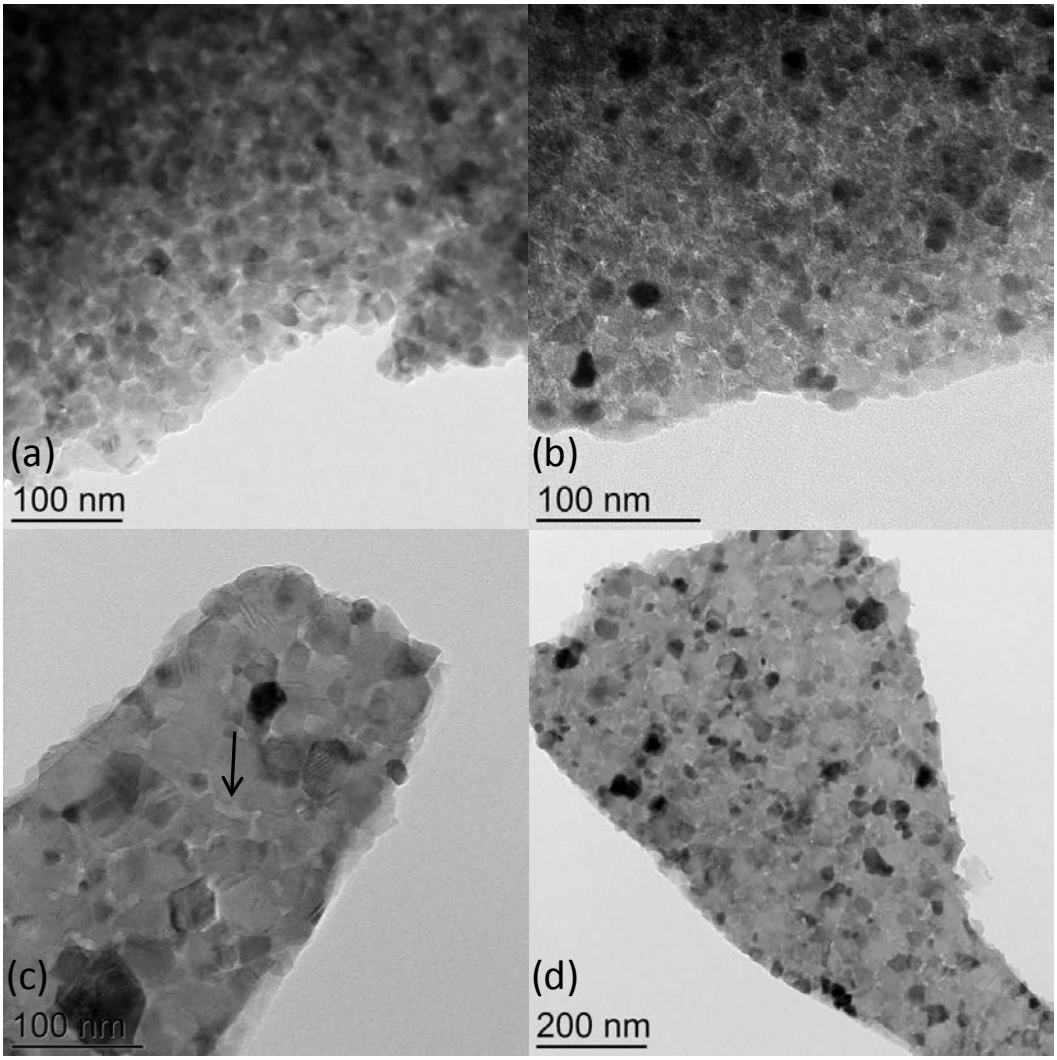

Figure 5 – Transmission electron micrographs of fresh $Ni_2Al_2O_5$ (a) $NiAl_4O_7$ (b) $NiAl_2O_4$ (c,d).

Table 2 – Average grain size calculated from dark field TEM image and sample composition from STEM-EDX mapping.

	Average grain size (nm)	**Average Ni content (mol %)**	**Average Al content (mol %)**	**Average O content (mol %)**	**Empirical formula from STEM-EDX**
$NiAl_4O_7$	14	9.3	37.8	52.9	$NiAl_4O_6$
$NiAl_2O_4$	23	12.4	26.7	60.9	$NiAl_2O_5$
$Ni_2Al_2O_5$	14	22.5	24.6	52.9	$Ni_2Al_2O_4$

X-ray Photoelectron Spectroscopy

X-ray photoelectron (XPS) spectra were obtained for fresh aluminate samples (Figure S10). The Ni 2p scan revealed two main peaks, $Ni2p_{3/2}$ and $Ni2p_{1/2}$, and their respective satellite peaks. The splitting of the main peak is due to "spin-orbit coupling" between the electron spin and the angular momentum vector.[54] The satellite peaks next to the main peaks occur because there are two final states with different occupation of 3d orbitals due to 4s – 3d interactions.[3] Gardner et al. studied Ni substituted aluminates by XPS and found that separation between the satellite peak and the main peak of 6.3 ± 0.3 eV is due to Ni bound in the aluminate structure and that a separation of 7.1 ± 0.1 eV is due to Ni in NiO. The main peaks in our samples had a separation from the satellite peak of 6.3 ± 0.1 eV, which indicated that surface nickel was primarily in the form of the aluminate structure. A binding energy (BE) of 531.3 eV was found for oxygen in $NiAl_2O_4$, and the O1s BE increased with increasing oxygen content. In all samples, the Ni/Al ratio was found to be about 5 times lower than the theoretical ratio (Table 3), which may indicate that a certain fraction exists in a nickel deficient aluminum-oxygen rich phase deposited on the surface of the $NiAl_2O_4$ spinel.[9]

Table 3 – Surface compositions of fresh catalysts determined by XPS.

	Ni $2p_{3/2}$ BE (eV)	**O1s BE (eV)**	**Al 2p BE (eV)**	**Ni/Al Experimental**	**Ni/Al Theoretical**
$NiAl_4O_7$	856.3	531.5	74.8	0.04	0.25
$NiAl_2O_4$	856.3	531.3	74.6	0.11	0.5
$Ni_2Al_2O_5$	856.2	531.1	74.6	0.21	1.0

Methane Dry Reforming and Methane Steam Reforming Reactivity

$NiAl_4O_7$, $NiAl_2O_4$, $Ni_2Al_2O_5$, and a commercial 50 wt% Ni/α-Al_2O_3 catalyst from Alfa Aesar were tested for methane dry reforming activity at 700 °C. The activity of the samples was tested starting in an unreduced and reduced state prior to reaction. Methane conversion over active samples after 6 h on stream is reported in Table 4. $NiAl_4O_7$ was active for methane dry reforming when reduced prior to reaction (Figure 6a) and had stable conversion of both methane and carbon dioxide over the time period examined. Unreduced $NiAl_4O_7$ had low but increasing conversion. $NiAl_2O_4$ was active for methane dry reforming in the reduced and unreduced state (Figure 6b). The conversion over reduced $NiAl_2O_4$ decreased relative to the initial conversion by 6% (X_{CO_2final}= 61%) for carbon dioxide and 8% (X_{CH_4final}=24%) of methane. Unreduced $NiAl_2O_4$ had stable a carbon dioxide conversion and a decrease in methane conversion of 8% (X_{CH_4final}=24%). The H_2/CO ratio obtained during methane dry reforming over $NiAl_2O_4$ in the reduced and unreduced state was found to 0.8. For reduced $NiAl_4O_7$ the ratio was 0.9. $Ni_2Al_2O_5$ and commercial 50 wt% Ni/α-Al_2O_3 were very active for methane conversion under dry reforming conditions, but rapid coking required a reactor shut down.

The catalysts were also evaluated for steam reforming at 700 °C starting in unreduced and reduced states. $Ni_2Al_2O_5$ was active for methane steam reforming when it was unreduced or reduced prior to reaction (Figure 7). The conversion of methane decreased relative to the initial conversion by only 7% ($X_{CH_{4final}}$=75%) to a value of for reduced $Ni_2Al_2O_5$ and 2% ($X_{CH_{4final}}$=76%) for unreduced $Ni_2Al_2O_5$ over 12 h on stream. $NiAl_2O_4$ was active for methane steam reforming when reduced prior to reaction (Figure 7), and methane conversion decreased by 2% over 12 h ($X_{CH_{4final}}$=76%). The commercial 50 wt% Ni/α-Al_2O_3 also showed sustained activity for methane steam reforming when unreduced prior to reaction, and the conversion of methane decreased by 1% ($X_{CH_{4final}}$=84%) over 12 h on stream. The conversion over commercial 50 wt% Ni/αAl_2O_3 after 6 h on stream ($X_{CH_{4initial}}$ = 85%) was slightly greater than that of the nickel aluminates ($X_{CH_{4initial}}$ = 78-83%). However, the hydrogen concentration was higher than the detection limit of the online GC indicating the H_2/CO ratio was extremely high. The H_2/CO ratio obtained for methane steam reforming over nickel aluminates was approximately 5 for unreduced $Ni_2Al_2O_5$ and reduced $NiAl_2O_4$. For $Ni_2Al_2O_5$ reduced prior to reaction, the H_2/CO ratio was approximately 4.

Table 4 – Methane conversion over $NiAl_4O_7$, $NiAl_2O_4$, $Ni_2Al_2O_5$, and commercial 50 wt% Ni/α-Al_2O_3 at 700 °C after 6 h on stream for methane steam reforming and methane dry reforming.

	X_{CH_4}[a] (%) Initial/Final			
	Reduced CH_4 Dry Reforming	Unreduced CH_4 Dry Reforming	Reduced CH_4 Steam Reforming	Unreduced CH_4 Steam Reforming
$NiAl_4O_7$	43	12	Not active	Not active
$NiAl_2O_4$	32	32	78	Not active
$Ni_2Al_2O_5$	Rapidly coked[b]	Rapidly coked[b]	82	78
50 wt% Ni/αAl_2O_3	Coked[c]	Rapidly coked[b]	Rapidly coked[b]	85

[a] **Methane conversions are assessed at t = 6h**
[b] **Coked requiring reactor shutdown at t < 1h**
[c] **Coked requiring reactor shutdown at t = 3h**

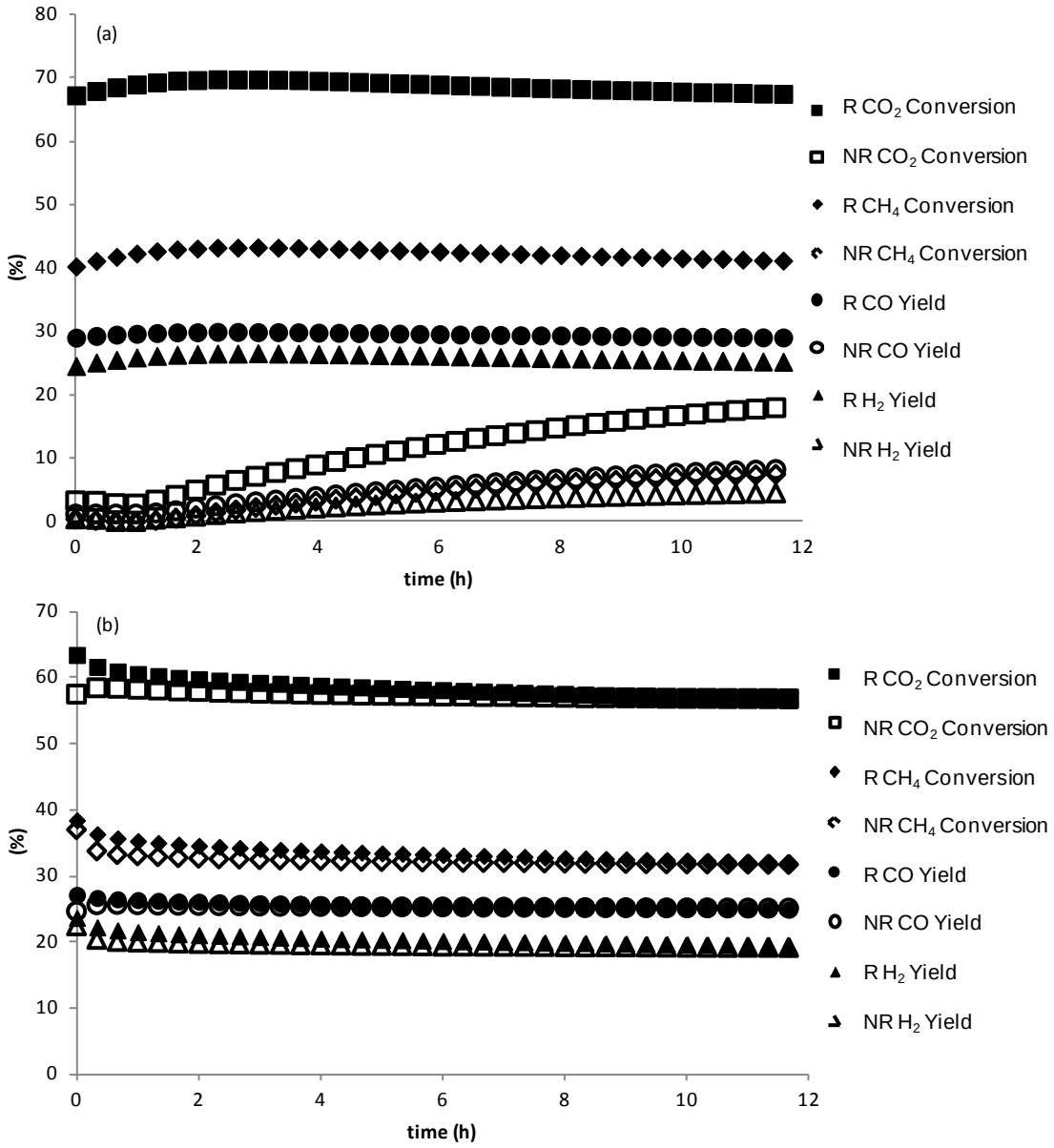

Figure 6 – CO_2/ CH_4 conversion and H_2/CO yield for methane dry reforming reaction at 700 °C, 1:1 CH_4:CO_2, reduced at 600 °C (2h) prior to reaction (R), unreduced prior to reaction (NR) for (a) $NiAl_4O_7$ and (b) $NiAl_2O_4$.

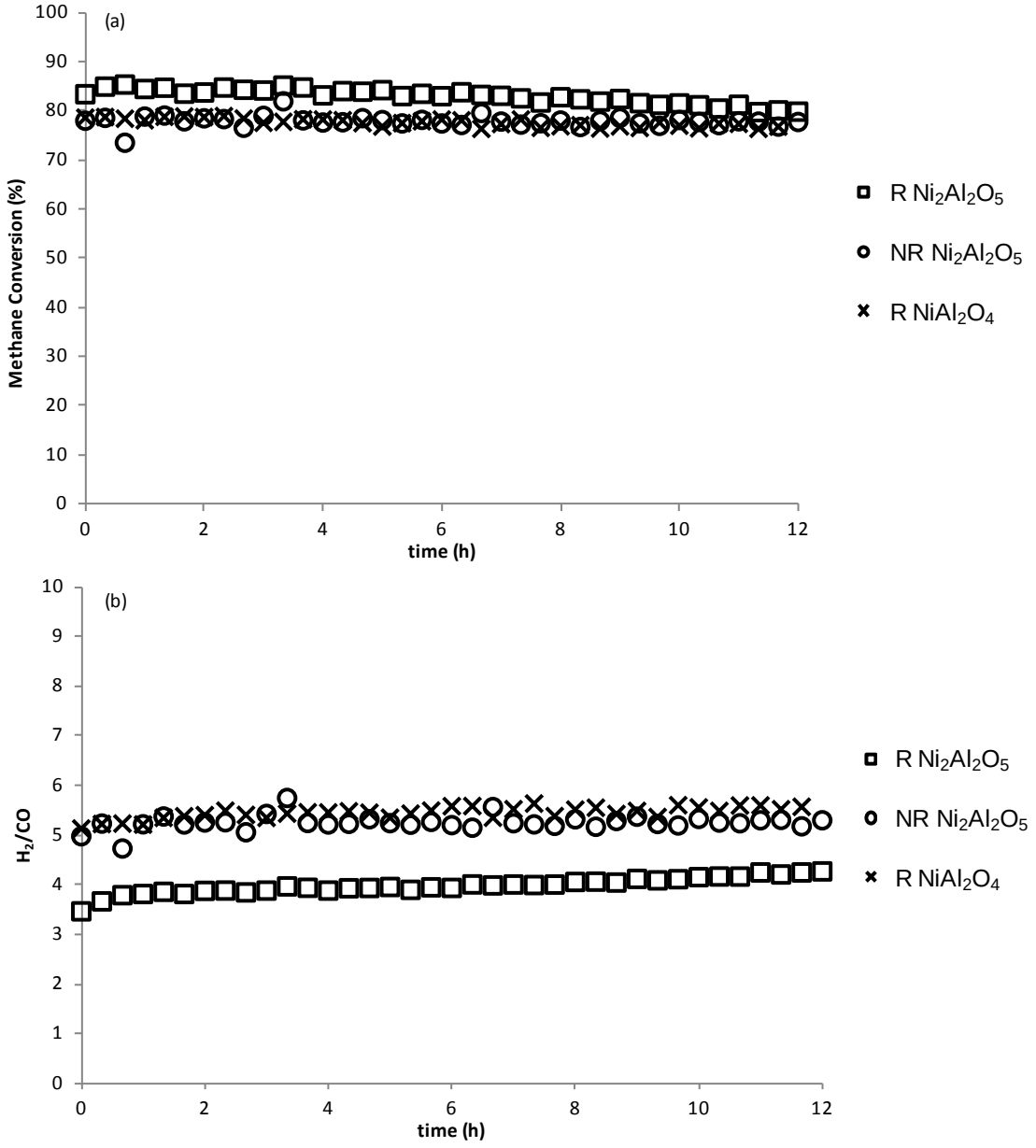

Figure 7 – (a) Methane conversion and (b) H_2/CO ratio methane steam reforming at 700 °C, S/C = 2.4, for $Ni_2Al_2O_5$ and $NiAl_2O_4$ reduced at 600 °C (2h) prior to reaction (R), unreduced prior to reaction (NR).

Carbonaceous Deposits

The carbon content on spent catalysts that were active and sufficiently stable for methane steam reforming and methane dry reforming was determined (Table 5). After methane dry reforming, nickel aluminates had carbon contents between 2.8 - 12.6 wt%. The commercial 50 wt% Ni/α-Al_2O_3 had a carbon content of 79 wt% when reduced prior to reaction after as short as 3 h on stream. For methane steam reforming, nickel aluminates had carbon contents of less than 1.0 wt%, and the commercial 50 wt% Ni/αAl_2O_3 had a carbon content of 10.9 wt%.

Table 5 – Carbon analysis of spent samples utilized in 12 h reactor experiments.

Amount of Carbonaceous Deposits on Spent Samples (wt% C)

	Reduced CH_4 Dry Reforming	Unreduced CH_4 Dry Reforming	Reduced CH_4 Steam Reforming	Unreduced CH_4 Steam Reforming
$NiAl_4O_7$	5.0	2.8	ND[a]	ND[a]
$NiAl_2O_4$	12.6	7.5	1.1	ND[a]
$Ni_2Al_2O_5$	ND[b]	ND[b]	<0.5	<0.5
50 wt% Ni/αAl_2O_3	79.0[c]	ND[b]	ND[b]	10.9

[a] Not determined (ND) because samples were not active.
[b] Not determined (ND) because samples coked causing reactor shutdown at t < 1h.
[c] Reactor was shut down at t = 3h due to coking. The carbon content was determined for comparative purposes.

X-ray Absorption Spectroscopy (XAS)

XANES spectra of $NiAl_4O_7$, $NiAl_2O_4$, and $Ni_2Al_2O_5$ after reduction at 900 °C are presented in Figure 8a. The white line intensity of the Ni K edge, which is indicative of the coordinative environment of Ni species, increased in the following order: $Ni_2Al_2O_5$ < $NiAl_2O_4$ <

$NiAl_4O_7$. Further, the Ni^{2+} pre-edge is not easily observed in any of the samples indicating reduction to metallic nickel. Linear combination fitting of the XANES region showed that $Ni_2Al_2O_5$ was completely reduced, $NiAl_2O_4$ was 85% reduced, and $NiAl_4O_7$ was 65% reduced. The EXAFS curve fitting results for $NiAl_4O_7$ (Table 6), $NiAl_2O_4$ (Table 7), and $Ni_2Al_2O_5$ (Table 8) confirmed that after exposure to H_2 at 900 °C metallic nickel species were present. The true Ni-Ni coordination number of $NiAl_4O_7$, $NiAl_2O_4$, and $Ni_2Al_2O_5$ was found by normalizing the coordination number of Ni-Ni found in the EXAFS fitting by the fraction of metallic Ni found from the linear combination fitting of the XANES. After determination of the true Ni-Ni coordination number, the nickel nanoparticle size present in reduced samples can be estimated.[55] $Ni_2Al_2O_5$ was estimated to have nickel nanoparticles of approximately 3 - 4 nm, $NiAl_2O_4$ 6 - 7 nm, and $NiAl_4O_7$ 8 - 10 nm. After reduction, the samples were oxidized at 900 °C. After oxidation, the Ni-O coordination number was found to return to the value found in the fresh samples. The coordination numbers for fresh and re-oxidized samples were approximately 5, 4.5, and 4 for $NiAl_4O_7$, $NiAl_2O_4$, and $Ni_2Al_2O_5$, respectively.

The oxidation state of nickel aluminates after exposure to methane dry reforming reaction conditions was also investigated (Figure 8b-d). The designation ‘Sample-NR’ is used when the sample was not subjected to a reductive pretreatment prior to exposure to reaction conditions and the designation ‘Sample-R’ is used for samples that were reduced in H_2 at 500 °C t prior to exposure to reaction conditions (Table 6-8). Linear combination fitting of the XANES region using NiO and Ni foil as references indicated that after dry reforming $Ni_2Al_2O_5$-NR contained 90% $Ni^{2+}$and 10% Ni^0. After reduction at 500 °C, $Ni_2Al_2O_5$-R was composed of 10% Ni^{2+} and 90% Ni^0, but this catalyst was partially oxidized to 30% Ni^{2+} and 70% Ni^0 after exposure to dry reforming reaction conditions (Table 8). After dry reforming, $NiAl_2O_4$-NR contained only Ni^{+2}

as evidenced from the pre-edge of the XANES, however, this did could not be fit with a NiO XANES reference. After 500 °C reduction the catalyst contained 40% Ni^{2+} and 60% Ni^0, which was partially oxidized to 90% Ni^{2+} and 10% Ni^0 after subsequent exposure to methane dry reforming reaction conditions. In contrast, it was not possible to fit the spectra of $NiAl_4O_7$- NR, $NiAl_4O_7$-R, and $NiAl_2O_4$-NR with a linear combination of the spectra of Ni^0 and NiO despite a decrease in white line intensity. The pre-edge features in the XANES region of these samples indicated the presence of Ni^{+2} species with a XANES shape different from that of NiO. Therefore, the reduction of the white line intensities during methane dry reforming is attributed to a change in the coordination sphere of Ni^{2+} species which remain part of the oxide phase.

To gain further insight into the changes in structure of nickel aluminates during methane dry reforming, difference spectra were created. This was achieved by subtracting the EXAFS region of the spectrum of the fresh sample from the spectrum after methane dry reforming (Figure S11). EXAFS fitting of the difference spectrum using a Ni foil standard indicated a Ni-Ni coordination number of 0.6 in $Ni_2Al_2O_5$-NR, a trace of metallic Ni in $NiAl_2O_4$-NR, and no metallic Ni was observed in $NiAl_4O_7$-NR (Figure 9). The true coordination number is determined by dividing the experimental coordination number by the fraction of metallic Ni determined from the XANES. Thus, the true coordination number of metallic Ni in $Ni_2Al_2O_5$ -NR is approximately 6 since only 10% of the nickel was present as nickel nanoparticles. From the true coordination number, the nickel nanoparticles sizes are estimated to be 1-2 nm.[55] $NiAl_2O_4$-NR contained little or no Ni-Ni coordination after exposure to reaction conditions, so the difference spectra were fit using a Ni-O scattering path (Figures S11 – S14). For $NiAl_2O_4$-R, the sample was found to contain a higher amount of metallic nickel than $NiAl_2O_4$-NR, which explains the

increase in the amount of carbonaceous deposits observed for this sample when it is reduced prior to exposure to reaction conditions.

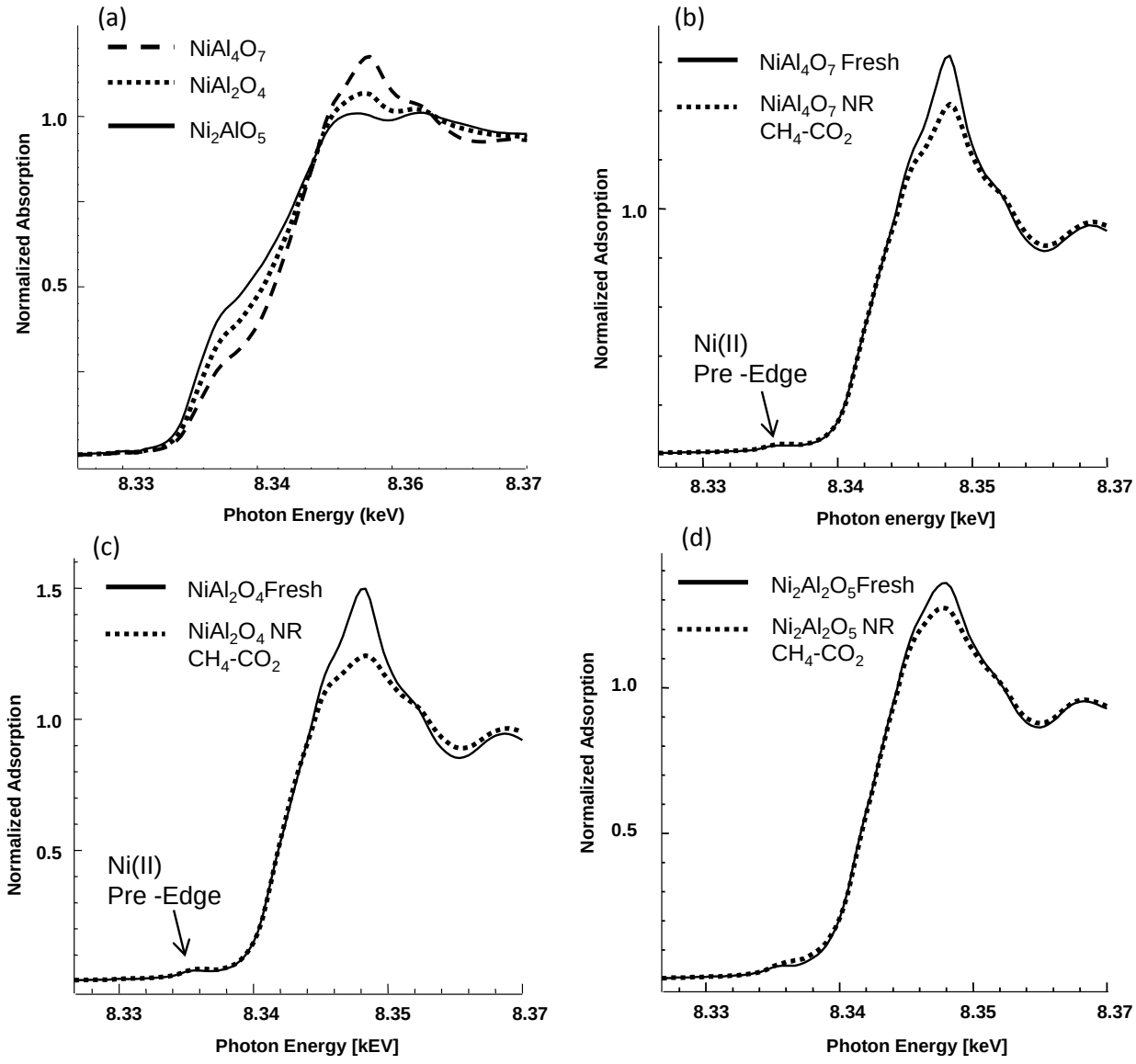

Figure 8 –Ni K-edge XANES from 8.32 to 8.37 keV of $NiAl_4O_7$, $NiAl_2O_4$, $Ni_2Al_2O_5$ (a) after reduction at 900°C. (b-d) fresh samples and after exposure to methane dry reforming (CH_4-CO_2) reaction conditions at 700 °C. Samples unreduced (NR) prior to exposure to reaction gas.

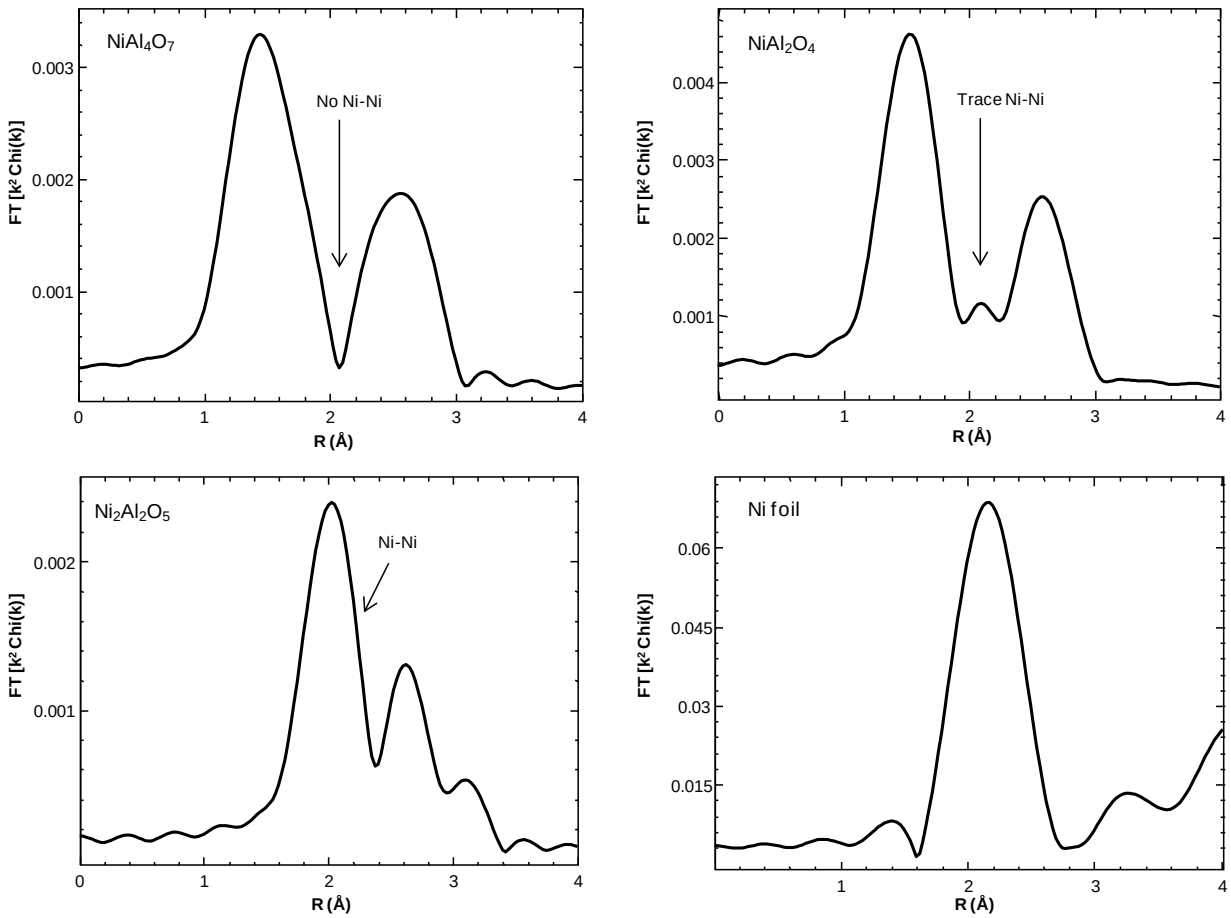

Figure 9 - Ni K-edge FT of the difference EXAFS of nickel aluminates as synthesized minus catalyst after exposure to methane dry reforming (CH_4 + CO_2) reaction conditions, NR.

Table 6 - Curve fitting results for the Ni-K edge EXAFS of the $NiAl_4O_7$.

Treatment	XANES Fraction		Scatter	N	R, Å	$\Delta\sigma^2$ (x 10^3)	Eo, eV	Comment
	Ni^{+2}	Ni^0						
As Is	1.0	-	Ni-O	5.1	2.06	0.0	-5.0	
900 H_2	0.4	0.6	Ni-O	2.0	2.05	0.0	4.4	8–10 nm
			Ni-Ni	7.5[a]	2.50	0.0	0.9	
900 O_2	1.0	-	Ni-O	5.4	2.08	5.0	0.4	
CH_4 –CO_2 Reforming 700 °C NR	1.0	-	Ni-O	4.6	2.06	0.0	-1.0	Change in Ni-O No Ni^0
500 °C H_2 pretreatment	0.4	0.6	Ni-O	1.8	2.06	0.0	-5.0	>10 nm Ni^0
			Ni-Ni	7.3[a]	2.49	0.0	-13.7	
CH_4 –CO_2 Reforming 700 °C R	1.0	-	Ni-O	5.0	2.06	0.0	-5.3	500 °C H_2 pretreatment

[a] **Calculated using empirical correlation of H_2 chemisorption and EXAFS CN for Platinum[55]**

Table 7 - Curve fitting results for the Ni-K edge EXAFS of the $NiAl_2O_4$.

Treatment	XANES Fraction		Scatter	N	R, Å	$\Delta\sigma^2$ (x 10^3)	Eo, eV	Comment
	Ni^{+2}	Ni^0						
As Is	1.0	-	Ni-O	4.4	2.07	0.0	-5.0	
900 H_2	0.15	0.85	Ni-Ni	8.9[a]	2.50	1.0	0.3	6-7nm Ni^0
900 O_2	1.0	-	Ni-O	4.5	2.07	0.4	-1.8	
CH_4 –CO_2 Reforming 700 °C NR	1.0	-	Ni-O	3.6	2.07	0.0	-0.4	Change in Ni-O Trace Ni^0
			Ni-O Difference	1.0[b]	2.06	0.0	-1.1	
500 °C H_2 pretreatment	0.4	0.6	Ni-O	1.8	2.07	0.0	-5.2	>10 nm Ni^0
			Ni-Ni	7.1[a]	2.49	0.0	-13.8	
CH_4 –CO_2 Reforming 700 °C R	0.9	0.1	Ni-O	3.9	2.08	0.0	-5.0	500 °C H_2 pretreatment Trace metallic Ni
			Ni-Ni Difference	2.1[a,b]	2.49	4.0	-13.2	

[a] Calculated using empirical correlation of H_2 chemisorption and EXAFS CN for Platinum[55]

[b] Difference spectrum created by subtracting the spectrum of the fresh sample from the spectrum of the sample after exposure to described experimental conditions.

Table 8 - Curve fitting results for the Ni-K edge EXAFS of the $Ni_2Al_2O_5$.

Treatment	XANES Fraction		Scatter	N	R, Å	$\Delta\sigma^2$ (x 10^3)	Eo, eV	Comment
	Ni^{+2}	Ni^0						
As Is	1.0	-	Ni-O	4.2	2.09	1.0	0.2	
900 H_2	-	1.0	Ni-Ni	8.5[a]	2.49	1.0	0.7	3-4 nm Ni^0
900 O_2	1.0	-	Ni-O	3.7	2.10	0.0	0.6	
CH_4 –CO_2 Reforming 700 °C NR	0.9	0.1	Ni-O	4.0	2.09	1.0	0.4	1-2 nm Ni^0
			Ni-Ni	6.0[a,b]	2.45	5.0	-12.7	
500C H_2 pretreatment	0.1	0.9	Ni-Ni	9.1[a]	2.49	0.0	-13.8	7-8 nm Ni^0
CH_4 –CO_2 Reforming 700 °C R	0.3	0.7	Ni-O	3.9	2.08	0.0	-5.0	3-4 nm Ni^0
			Ni-Ni	5.8[a,b]	2.49	1.0	-13.5	

[a] **Calculated using empirical correlation of H_2 chemisorption and EXAFS CN for Platinum[55]**

[b] **Difference spectrum created by subtracting the spectrum of the fresh sample from the spectrum of the sample after exposure to described experimental conditions.**

Discussion

Formation of Nickel Aluminates

The formation of a rigid polymeric resin during Pechini synthesis allows for formation of highly uniform nickel aluminates because the diffusion of metal ions during the synthesis is reduced by gradual decomposition of the resin.[47,56,57]

The nickel aluminates prepared in the present study had moderate surface areas (25 – 40 m^2/g) and were mesoporous allowing reactants to access a significant part of the material. The grain size of fresh samples found from TEM ranges from 14 – 23 nm. As expected, STEM-EDX analysis indicated nanoscale stoichiometry similar to bulk stoichiometry determined by ICP. However, XPS, which only analyzes the sample up to a depth of about 5 nm,[58] showed that these materials have an aluminum and oxygen rich surface at room temperature. In agreement with

previous studies,[47,56,57] our results indicate that the Pechini synthesis provides materials that have uniform compositions, high degree of crystallinity, and small grain sizes. In contrast, synthesis of stoichiometric $NiAl_2O_4$ by solid state reaction was found to produce a material with several types of NiO in addition to bulk $NiAl_2O_4$.[9] The non-uniform catalysts severely sintered and formed large quantities of carbonaceous deposits during catalytic methane decomposition. In contrast to the current study, synthesis of $NiAl_2O_4$ by solid state reaction produced a catalyst with several NiO species that sintered and coked during methane reforming.

Mobility of Nickel Species in Nickel Aluminates

Materials that are similar to nickel aluminates have shown unique regenerative capabilities. Nishihata et al. studied Pd perovskites prepared by the alkoxide method for automotive emissions control.[23] It was found that Pd was able to move out of the perovskite lattice under reducing conditions and back in its original position in an oxidizing atmosphere giving it high catalytic activity and a long lifetime. In a separate study by Kizaki et al., $La(Fe_{1-x}Pd_x)O_3$ perovskites prepared by the alkoxide method were found to have excellent stability and activity for automotive emissions control due to nanospinodal decomposition.[24] In nanospinodal decomposition, the perovskite decomposes into $LaFeO_3$ and $PdFeO_3$ at high temperatures, but the crystal structure itself is maintained. Li et al. examined Ni-Fe-Mg-Al-O catalysts prepared by co-precipitation for tar reforming of biomass derived syngas.[8] Under reducing conditions, uniform Ni-Fe nanoparticles were formed from the bulk mixed oxide, and under oxidizing conditions, the Ni-Fe nanoparticles were reincorporated into the bulk structure.

In the present study, TPR/TPO, XRD, and XAS demonstrated the regeneration potential of nickel aluminates at high temperatures in terms of reversible changes of their oxidation state.

All samples were almost fully reduced (TPR), re-oxidized (TPO), and then re-reduced (TPR2). The TPR profiles showed $NiAl_4O_7$ and $NiAl_2O_4$ had predominantly high temperature reduction peaks associated with reduction of bulk nickel aluminate. NiO, as well as bulk nickel aluminates, were reduced in $Ni_2Al_2O_5$. The presence of NiO was indicated by the low temperature reduction peak. The broad TPO patterns indicated there were several types of oxygen acceptor sites present within the samples. TPR2 showed that the reduction peak temperatures were only slightly increased, which indicated that the mobility of nickel was only slightly reduced after repeated exposure to high temperatures. The low temperature region of the TPR2 profile of $Ni_2Al_2O_5$ was dominated by a peak around 340 °C instead of the bimodal peak observed for the fresh sample, which is likely due to agglomeration of nickel oxide nanoparticles on the aluminate surface creating somewhat larger nickel nanoparticles. XRD was performed on samples after each TPR/TPO treatment and demonstrated the mobility of nickel particles out of the host framework by the ability of the materials to return to a structure similar to their initial structure under conditions more severe than those used during reactivity studies. XAS analysis complemented TPR/TPO and XRD results. Specifically, XANES indicated that after reduction at 900 °C, $NiAl_4O_7$ can be 65% reduced, $NiAl_2O_4$ can be 85% reduced, and $Ni_2Al_2O_5$ can be 100% reduced. After oxidation at 900 °C, the Ni-O coordination number of nickel aluminates was the same as in the fresh samples. We conclude that the ability of these materials to return to their initial state after exposure to oxidizing and reducing conditions at high temperature indicates their potential application for many high temperature reactions such as methane steam reforming and methane dry reforming.

Active Site for Methane Steam and Dry Reforming and their Role in Carbon Formation

Methane dry reforming occurs according to the stoichiometric equation[59,60]

$CH_4 + CO_2 \leftrightarrow 2CO + 2H_2$ $\Delta H^0_{298K} = 247$ kJ/mol (1)

while methane steam reforming (Equation 2) follows the equation

$CH_4 + H_2O \leftrightarrow CO + 3H_2$ $\Delta H^0_{298K} = 206$ kJ/mol (2)

The water gas shift (Equation 3) reaction and formation of carbonaceous species (Equation 4,5,6) can also occur under the experimental conditions and can have significant impact on the target reactions (Equations 1,2).

$CO + H_2O \leftrightarrow CO_2 + H_2$ $\Delta H^0_{298K} = 41$ kJ/mol (3)

$CH_4 \leftrightarrow C + 2H_2$ $\Delta H^0_{298K} = 75$ kJ/mol (4)

$2CO \leftrightarrow C + CO_2$ $\Delta H^0_{298K} = -171$ kJ/mol (5)

$CO + H_2 \leftrightarrow C + H_2O$ $\Delta H^0_{298K} = -131$ kJ/mol (6)

H_2/CO ratios of less than unity during methane dry reforming are commonly attributed to the inverse water gas shift reaction.[61] H_2/CO ratios from 3 to 16 have been observed during methane steam reforming and can be attributed to the forward water gas shift reaction.[13] The different direction of the water gas shift (Equation 3) during methane steam reforming and methane dry reforming, respectively, results from the different composition of the feed for these reactions.

Methane steam reforming has been proposed to proceed via dehydrogenation of methane to form surface carbon, which is oxidized by adsorbed oxygen from water dissociation.[14] Methane dry reforming is thought to proceed via decomposition of methane to form surface

carbon and hydrogen, and reaction of surface carbon with carbon dioxide.[20] Fundamentally, the mechanism of methane steam reforming and methane dry reforming may not be significantly different.[61] However, the thermodynamics of methane dry reforming favor formation of nickel carbide or carbon, while methane steam reforming favors the formation of nickel or nickel oxide.[61] Deng et al. showed that $LaPrFeNiO_3$ catalysts prepared by a modified Pechini synthesis were deactivated by formation of stable, filamentous carbon during dry reforming, while during oxidative methane reforming (CH_4:CO_2:O_2 = 1:0.7:0.3) no carbonaceous deposits were observed.[16] Under reducing conditions, Ni deficient nickel aluminates prepared by the sol-gel method formed dispersed nickel nanoparticles that were active for methane steam reforming.[13] Due to the small size of these particles, carbon formation was very low. Similarly, it was reported that $NiAl_2O_4$ prepared by a sol-gel had high dry reforming activity with limited coke formation due to the formation of small metal particles that form from the aluminate structure at the same temperature of the catalytic reaction.[21]

Many studies using nickel catalysts reported that the active species in reforming reactions are the reduced nickel metal particles.[8,9,19,21,41] Our study found that $NiAl_2O_4$ was active for methane dry reforming in the unreduced and reduced states. Reduced $NiAl_4O_7$ was immediately active for methane dry reforming, and the conversion of methane and carbon dioxide was higher than that over $NiAl_2O_4$ in either the reduced or unreduced state. The absence of metallic Ni in non-reduced or reduced $NiAl_4O_7$ and low amount of metallic nickel present in non-reduced or reduced $NiAl_2O_4$ during methane dry reforming provides strong evidence that the active site responsible for stable activity is an oxide. It is speculated that in the case of reduced $NiAl_4O_7$, the reduction facilitates the formation of accessible fourfold coordinated nickel oxide species that are active and stable for methane dry reforming. Further, the activity of unreduced

$NiAl_4O_7$ was low and slowly increased during time on stream because it takes longer for the Ni atoms to migrate to an environment with a Ni-O coordination number around 4 where they are accessible and catalytically active. In the case of $NiAl_2O_4$, the coordination of the as-synthesized oxide was close to 4, which explains the observation of the same activity for methane dry reforming in reduced and unreduced samples. Fourfold coordinated oxidic nickel species can be present in square planar geometry, which would allow for nickel in such coordination to be accessible to reactants.[62] In a related study, tetrahedrally coordinated nickel was proposed as an active site for low weight loading Ni/Al_2O_3 catalysts in the highly selective oxidative dehydrogenation of ethane to ethylene.[63]

Importantly, the active oxide, presumably fourfold coordinated Ni^{2+}species, appears to play little to no part in the formation of carbonaceous deposits. The formation of such deposits is enhanced when reduced nickel particles are present. Specifically, $NiAl_4O_7$-R and $NiAl_2O_4$-R/NR had only trace amounts of metallic Ni at the beginning of the reaction (Table 6-7) and formed limited amounts of carbonaceous deposits during dry reforming (Table 5). Deactivation of stable nickel aluminates was less than 6% of carbon dioxide and 8% of methane during 12 h on stream, and the H_2/CO ratio was very close to unity.

During the dry reforming reaction over $Ni_2Al_2O_5$, 10% of the Ni was reduced to nickel nanoparticles of 1 – 2 nm when the sample was not reduced prior to reaction (Table 8) and 70% of the Ni was reduced to nickel nanoparticles of 1 - 2 nm when the sample was reduced prior to reaction. The rapid accumulation of carbonaceous deposits on this catalyst indicated that the presence of metallic nickel favors the formation of substantial amounts of carbon deposits. Similar to $Ni_2Al_2O_5$, the commercial 50 wt% Ni/α-Al_2O_3 catalyst accumulated substantial amounts of deposits (79 wt% carbon in only 3 h on stream), which is attributed to the presence of

metallic Ni particles. Note that the formation of carbonaceous deposits on metallic nickel is thermodynamically favored under methane dry reforming conditions and that this reaction appears to involve nickel carbide/carbon species as intermediates. In summary, these results indicate reduced $NiAl_4O_7$ contained the right proportion of fourfold coordinated nickel to provide optimal performance for methane dry reforming while limiting carbon formation.

In the case of methane steam reforming, reduced nickel nanoparticles are the active phase.[14] Reduced and unreduced $Ni_2Al_2O_5$ as well as reduced $NiAl_2O_4$ were active for methane steam reforming and had H_2/CO ratios between 4 and 5. The slightly lower methane conversion of the unreduced $Ni_2Al_2O_5$ and reduced $NiAl_2O_4$ is attributed to lower densities of nickel nanoparticles relative to reduced $Ni_2Al_2O_5$. This is in agreement with *in-situ* XRD measurement, which indicated the formation of metallic nickel in $Ni_2Al_2O_5$ in hydrogen at temperatures as low as 650 °C. Reduced $NiAl_2O_4$ is believed to exhibit activity for methane steam reforming because of an increase in metallic nickel as metallic nickel particles >10 nm were observed for $NiAl_2O_4$ reduced at 500 °C from XAS. It is speculated that unreduced $NiAl_2O_4$ was not active for methane steam reforming because it only had few or no nickel nanoparticles, as indicated by the XAS results of this unreduced sample during methane dry reforming. XAS measurements showed that 10% of the Ni in $Ni_2Al_2O_5$ was reduced during methane dry reforming. We speculate that a similar amount of reduced nickel nanoparticles exists when $Ni_2Al_2O_5$ is used for methane steam reforming without prior reduction. When $Ni_2Al_2O_5$ is reduced at 500 °C it was found to contain 90% Ni^0 nickel and nanoparticles of 7-8 nm exist which can explain the higher activity observed for $Ni_2Al_2O_5$-R. Carbon formation was very low on active aluminate samples, which could indicate the nickel nanoparticles remained small throughout the reaction, as carbon nucleation requires nickel particles of a certain size.[21] Unreduced commercial 50 wt% Ni/α-Al_2O_3 was

slightly more active than the nickel aluminates. However, the H_2/CO ratio was extremely high, which is an undesirable result if the syngas product is to be used for anything other than hydrogen production. The conversion of methane decreased during the 12 h study by less than 7% for all samples. The commercially available 50 wt% Ni/α-Al_2O_3 catalyst formed 10 times the amount of carbonaceous deposits compared to the active nickel aluminates. These results indicate that reduced $Ni_2Al_2O_5$ provides optimal performance for methane steam reforming while limiting the formation of carbon.

Conclusions

Nickel aluminates prepared by Pechini synthesis are excellent candidates for high temperature reforming reaction catalysts. Physicochemical characterization revealed unique structural properties, indicated a high degree of mobility of nickel in the aluminate structure, and demonstrated the regeneration properties of nickel aluminates under harsh reaction conditions. The minimal change to the materials upon redox cycling, as seen by TPRs and TPO, indicates that it may be possible to regenerate these materials after some level of coking has occurred. Fourfold coordinated nickel species on $NiAl_4O_7$ and $NiAl_2O_4$ are identified as potential active sites for methane dry reforming providing high and stable activity. These sites form few carbonaceous deposits under dry reforming conditions, whereas significant amounts of such deposits are formed on the metallic nickel particles present in reduced $NiAl_2O_4$ and unreduced/reduced $Ni_2Al_2O_5$. The metallic nickel nanoparticles that cause the formation of deposits in methane dry reforming are believed to be the active sites for methane steam reforming. Reduced $NiAl_2O_4$ and unreduced/reduced $Ni_2Al_2O_5$ had high and stable activity

during methane steam reforming studies. In contrast to dry reforming, reduced nickel particles are the active sites for this reaction.

Funding Sources

The work was funded by The Dow Chemical Company and a fellowship from the Renewable Bioproducts Institute at the Georgia Institute of Technology. JTM and JRG were funded by the U.S. Department of Energy, Office of Basic Energy Sciences, Chemical Sciences under Contract DE-AC-02-06CH11357. Use of the Advanced Photon Source was supported by the U.S. Department of Energy, Office of Science, Office of Basic Energy Sciences, under Contract No. DE-AC02-06CH11357. Use of NSLS is supported by the U.S. DOE Grant No. DE-AC02-98CH10866.

Supporting Information

Equations for calculations of conversions and yields, TPR data, in-situ X-ray diffractograms, TEM diffraction patterns and images, HAADF-STEM-EDX results, X-ray photoelectron spectra, and EXAFS data. This material is available free of charge via the Internet at http://pubs.acs.org.

Acknowledgements

Derrick Flick, Brien Stears, Mark Siddoway, and Billy Bardin from the Dow Chemical Company are thanked for fruitful discussions. The assistance of Tianpin Wu at beamline 9-BM-C at Argonne National Laboratory in collecting XAS measurements is greatly appreciated (Proposal GUP-38563). The authors also wish to thank Yong Ding for acquiring TEM images. We thank Justin Notestein and Andrew Korinda for their help in orientation and data collection techniques

at Argonne National Laboratory. Rich discussions regarding XRD with Dr. Z. John Zhang are acknowledged. We would also like to thank Steven Ehrlich for his help with the synchrotron experiment.

References

(1) Yung, M. A.; Jablonski, W. S.; Magrini-Bair, K. A. *Energy Fuels* **2009**, *23*, 1874-1887.

(2) Sutton, D.; Kelleher, B.; Ross, J. R. H. *Fuel Process. Technol.* **2001**, *73*, 155-173.

(3) Winkler, A.; Borchert, H.; Al-Shamery, K. *Surf. Sci.* **2006**, *600*, 3036-3044.

(4) Muirhead-Gould, J. S.; Laidler, K. J. *T. Faraday Soc.* **1967**, *63*, 944-952.

(5) Ewbank, J. L.; Kovarik, L.; Diallo, F. Z.; Sievers, C. *Appl. Catal. A-Gen.* **2015**, *494*, 57-67.

(6) Bhattacharyya, A.; Chang, V. W. *Stud. Surf. Sci. Catal.* **1994**, *88*, 207-213.

(7) Xu, Z. L.; Zhen, M.; Bi, Y. L.; Zhen, K. J. *Appl. Catal. A-Gen.* **2000**, *198*, 267-273.

(8) Li, D.; Koike, M.; Wang, L.; Nakagawa, Y.; Xu, Y.; Tomishige, K. *Chemsuschem* **2014**, *7*, 510-522.

(9) Rivas, M. E.; Fierro, J. L. G.; Guil-Lopez, R.; Pena, M. A.; La Parola, V.; Goldwasser, M. R. *Catal. Today* **2008**, *133*, 367-373.

(10) Lo Jacono, M.; Schiavello, M.; Cimino, A. *J. Phys. Chem.* **1971**, *75*, 1044-1050.

(11) Bartholomew, C. H.; Farrauto, R. J. *J. Catal.* **1976**, *45*, 41-53.

(12) Ross, J. R. H.; Steel, M. C. F.; Zeiniisfahani, A. *J. Catal.* **1978**, *52*, 280-290.

(13) Salhi, N.; Petit, C.; Kiennemann, A. *Stud. Surf. Sci. Catal.* **2008**, *174*, 1335-1338.

(14) Alubaid, A.; Wolf, E. E. *Appl. Catal.* **1988**, *40*, 73-85.

(15) Chu, W. L.; Yang, W. S.; Lin, L. W. *Catal. Lett.* **2001**, *74*, 139-144.

(16) Deng, J.; Cai, M.; Sun, W.; Liao, X.; Chu, W.; Zhao, X. S. *Chemsuschem* **2013**, *6*, 2061-2065.

(17) Machida, M.; Eguchi, K.; Arai, H. *J. Catal.* **1989**, *120*, 377-386.

(18) Zhang, K.; Zhou, G. D.; Li, J.; Cheng, T. X. *Catal. Commun.* **2009**, *10*, 1816-1820.

(19) Ribeiro, N. F. P.; Neto, R. C. R.; Moya, S. F.; Souza, M. M. V. M.; Schmal, M. *Int. J. Hydrog. Energy* **2010**, *35*, 11725-11732.

(20) Gonzalez, A. R.; Asencios, Y. J. O.; Assaf, E. M.; Assaf, J. M. *Appl. Surf. Sci.* **2013**, *280*, 876-887.

(21) Sahli, N.; Petit, C.; Roger, A. C.; Kiennemann, A.; Libs, S.; Bettahar, M. M. *Catal. Today* **2006**, *113*, 187-193.

(22) Golpasha, R. D.; Karami, D.; Ahmadi, R.; Bagherzadeh, E. *React. Kinet. Catal. Lett.* **1993**, *51*, 393-400.

(23) Nishihata, Y.; Mizuki, J.; Akao, T.; Tanaka, H.; Uenishi, M.; Kimura, M.; Okamoto, T.; Hamada, N. *Nature* **2002**, *418*, 164-167.

(24) Kizaki, H.; Kusakabe, K.; Nogami, S.; Katayama-Yoshida, H. *Appl. Phys. Express* **2008**, *1*.
(25) Achouri, I. E.; Abatzoglou, N.; Fauteux-Lefebvre, C.; Braidy, N. *Catal. Today* **2013**, *207*, 13-20.
(26) Fauteux-Lefebvre, C.; Abatzoglou, N.; Braidy, N.; Achouri, I. E. *J. Power Sources* **2011**, *196*, 7673-7680.
(27) Skoufa, Z.; Xantri, G.; Heracleous, E.; Lemonidou, A. A. *Appl. Catal. A: Gen.* **2014**, *471*, 107-117.
(28) Gardner, T. H.; Shekhawat, D.; Berry, D. A.; Smith, M. W.; Salazar, M.; Kugler, E. L. *Appl. Catal. A-Gen.* **2007**, *323*, 1-8.
(29) Collongues, R.; Gourier, D.; Kahnharari, A.; Lejus, A. M.; Thery, J.; Vivien, D. *Annu. Rev. Mater. Sci.* **1990**, *20*, 51-82.
(30) Chu, W. L.; Yang, W. S.; Lin, L. W. *Appl. Catal. A-Gen.* **2002**, *235*, 39-45.
(31) Gardner, T. H.; Spivey, J. J.; Kugler, E. L.; Campos, A.; Hissam, J. C.; Roy, A. D. *J. Phys. Chem. C* **2010**, *114*, 7888-7894.
(32) Tejuca, L. G.; Fierro, J. L. G. *Properties and applications of perovskite-type oxides*; Marcel Dekker: New York, **1993**.
(33) Gaudon, M.; Robertson, L. C.; Lataste, E.; Duttine, M.; Menetrier, M.; Demourgues, A. *Ceram. Int.* **2014**, *40*, 5201-5207.
(34) Murthy, I.; Swamy, C. S. *J. Mater. Sci.* **1993**, *28*, 1194-1198.
(35) Han, Y. S.; Li, J. B.; Ning, X. S.; Chi, B. *J. Am. Ceram. Soc.* **2004**, *87*, 1347-1349.
(36) Han, Y. S.; Li, J. B.; Ning, X. S.; Yang, X. Z.; Chi, B. *Mater. Sci. Eng. A-Struct. Mater. Prop. Microstruct. Process.* **2004**, *369*, 241-244.
(37) Jose-Alonso, D. S.; Illan-Gomez, M. J.; Roman-Martinez, M. C. *Int. J. Hydrog. Energy* **2013**, *38*, 2230-2239.
(38) Zhang, Z. J.; Wang, Z. L.; Chakoumakos, B. C.; Yin, J. S. *J. Am. Chem. Soc.* **1998**, *120*, 1800-1804.
(39) Hamada, I.; Uozumi, A.; Morikawa, Y.; Yanase, A.; Katayama-Yoshida, H. *J. Am. Chem. Soc.* **2011**, *133*, 18506-18509.
(40) Katz, M. B.; Zhang, S.; Duan, Y.; Wang, H.; Fang, M.; Zhang, K.; Li, B.; Graham, G. W.; Pan, X. *J. Catal.* **2012**, *293*, 145-148.
(41) Enger, B. C.; Lodeng, R.; Walmsley, J.; Holmen, A. *Appl. Catal. A-Gen.* **2010**, *383*, 119-127.
(42) Jeevanandam, P.; Koltypin, Y.; Gedanken, A. *Nano Letters* **2001**, *1*, 263-266.
(43) Santiago, M.; Perez-Ramirez, J. *Environ. Sci. Technol.* **2007**, *41*, 1704-1709.
(44) Cui, H. T.; Zayat, M.; Levy, D. *J. Sol-Gel Sci. Technol.* **2005**, *35*, 175-181.
(45) Pechini, M., US patent 3,438,723, **1969**.
(46) Gama, L.; Ribeiro, M. A.; Barros, B. S.; Kiminami, R. H. A.; Weber, I. T.; Costa, A. *J. Alloy. Compd.* **2009**, *483*, 453-455.
(47) Kakihana, M.; Yoshimura, M. *Bull. Chem. Soc. Jpn.* **1999**, *72*, 1427-1443.
(48) Sing, K. S. W.; Everett, D. H.; Haul, R. A. W.; Moscou, L.; Pierotti, R. A.; Rouquerol, J.; Siemieniewska, T. *Pure Appl. Chem.* **1985**, *57*, 603-619.
(49) Stampfl, C. *Catal. Today* **2005**, *105*, 17-35.

(50) Ding, Y.; Liu, Y.; Niu, S. M.; Wu, W. Z.; Wang, Z. L. *J. Appl. Phys.* **2014**, *116*, 154304
(51) Zielinski, J. *J. Catal.* **1982**, *76*, 157-163.
(52) Lopez-Fonseca, R.; Jimenez-Gonzalez, C.; de Rivas, B.; Gutierrez-Ortiz, J. I. *Appl. Catal. A-Gen.* **2012**, *437*, 53-62.
(53) Williams, D.; Carter, B. *Transmission Electron Microscopy: A Textbook for Materials Science*, 2nd ed.; Springer: New York, **2009**.
(54) Briggs, D.; Heyden, E.; London, S. *Hanbook of X-ray and Ultraviolet Photoelctron Spectroscopy*; Heyden & Son London, **1977**.
(55) Miller, J. T.; Kropf, A. J.; Zha, Y.; Regalbuto, J. R.; Delannoy, L.; Louis, C.; Bus, E.; van Bokhoven, J. A. *J. Catal.* **2006**, *240*, 222-234.
(56) Liu, X. M.; Gao, W. L. *Mater. Manuf. Process.* **2012**, *27*, 905-909.
(57) Ferri, E. A. V.; Santos, I.; Radovanovic, E.; Bonzanini, R.; Girotto, E. M. *J. Braz. Chem. Soc.* **2008**, *19*, 1153-1157.
(58) Appapillai, A. T.; Mansour, A. N.; Cho, J.; Shao-Horn, Y. *Chem. Mat.* **2007**, *19*, 5748-5757.
(59) Zhang, J. G.; Wang, H.; Dalai, A. K. *J. Catal.* **2007**, *249*, 300-310.
(60) Xu, J.; Froment, G. F. *AIChE Journal* **1989**, *35*, 88-96.
(61) Wang, S. B.; Lu, G. Q. M.; Millar, G. J. *Energy Fuels* **1996**, *10*, 896-904.
(62) Wiberg, N.; Holleman, A. F.; Wiberg, E. *Inorganic Chemistry*; Academic Press: San Diego, **2001**.
(63) Heracleous, E.; Lee, A. F.; Wilson, K.; Lemonidou, A. A. *J. Catal.* **2005**, *231*, 159-171.

Table of Contents Figure